Improvements to Cloud-Top Brightness Temperatures Computed from the CRTM at 3.9 μm

Lewis Grasso

Cooperative Institute for Research in the Atmosphere, Colorado State University, Fort Collins, Colorado

Daniel T. Lindsey

NOAA/Center for Satellite Applications and Research, and Cooperative Institute for Research in the Atmosphere, Colorado State University, Fort Collins, Colorado

Yoo-Jeong Noh, Christopher O'Dell, and Ting-Chi Wu

Cooperative Institute for Research in the Atmosphere, Colorado State University, Fort Collins, Colorado

Fanyou Kong

Center for Analysis and Prediction of Storms, University of Oklahoma, Norman, Oklahoma

ABSTRACT

In preparation for all-sky satellite radiance assimilation, the Community Radiative Transfer Model (CRTM), version 2.1.3, was used to produce *Geostationary Operational Environmental Satellite-12/13* (*GOES-12/13*) imagery near 3.9 μm. For the current study, model output simulated from different models, microphysics, and weather events was used by the CRTM to generate imagery over and near the United States. A direct comparison of observed and CRTM *GOES-12/13* imagery near 3.9 μm revealed that CRTM brightness temperatures of solid-water cold cloud tops were approximately 30 K less than observed values. Two CRTM errors were identified and resolved: 1) a coding error that was found by the CRTM team and 2) incorrect optical properties of ice, resulting in improved values of brightness temperatures. Further, changes in microphysics also contributed to improvements, save for one case. The coding error solution appeared in the publicly released CRTM, version 2.3.0, on 27 November 2017, while the inclusion of the optical property solution is undetermined. Since the CRTM is the radiative transfer model within the operational data assimilation system at the National Centers for Environmental Prediction (NCEP), improvements to both the CRTM and model microphysics will be beneficial for future all-sky radiance assimilation activities.

1. Introduction

Assimilation of clear-sky satellite radiances began at the U.S. National Oceanic and Atmospheric Administration (NOAA) National Centers for Environmental Prediction (NCEP) approximately two decades ago. Derber and Wu (1998) assimilated clear-sky radiances from multiple sensors: 1) the High Resolution Infrared Radiation Sounder, 2) the Microwave Sounding Unit, and 3) the Stratospheric Sounding Unit. Clear-sky assimilation was done with the three-dimensional variational data assimilation (3DVAR) Spectral Statistical Interpolation (SSI; Parrish and Derber 1992), which incorporated the Radiative Transfer for the Television and Infrared Observation Satellite (TIROS) Operational Vertical Sounder (TOVS) (RTTOV; Saunders et al. 1999; Matricardi et al. 2004). The assimilation system was implemented operationally at NCEP on 25 October 1995.

Several years of operational use of the SSI 3DVAR system ended with the introduction of a new assimilation system. SSI was replaced by the Gridpoint Statistical Interpolation analysis system (GSI), which was implemented into the Global Data Assimilation System (GDAS) on 1 May 2007 at NCEP (Kleist et al. 2009).

Corresponding author: Lewis Grasso, lewis.grasso@colostate.edu

GSI takes advantage of formulating the assimilation problem in gridpoint space (Wu et al. 2002). Application of GSI ranges from not only the global scale, GDAS for example, but also to regional scales predicted by both the intermediate and innermost nests of the Hurricane Weather Research and Forecasting (HWRF) Model (Tallapragada et al. 2014) as reported by Wu et al. (2016) and Wu et al. (2018). In addition, an improved radiative transfer model was also incorporated into GSI: version 1 of the Community Radiative Transfer Model (CRTM; Han et al. 2006).

Over the past several years at NCEP, improved forecast skill has been obtained with the development of additional data assimilation systems. First, a GSI 3DVAR-based hybrid ensemble-variational assimilation system was developed by Wang et al. (2013). Results from their study showed improvements in wind, temperature, and specific humidity when compared to the operational GSI system (Wang et al. 2013). Second, Kleist and Ide (2015) developed a hybrid four-dimensional ensemble-variational system. Their results indicated improvement in forecasted heights and winds in extratropical regions.

Additional benefits have been recently reported by Zhu et al. (2016) with updates to GSI that allow for the assimilation of microwave radiances of nonprecipitating clouds over ocean-only scenes, which represents a significant step toward all-sky radiance assimilation. Subsequently, assimilation of clear and cloudy scenes from the microwave radiometer on the Advanced Microwave Sounding Unit-A platform became operational at NCEP on 12 May 2016.

One common component of the above data assimilation techniques was the use of the CRTM, which has forward, tangent linear, adjoint, and **K**-matrix versions. As a result, accurate calculations of top of the atmosphere radiances from the CRTM are essential for improved data assimilation. Since the release of version 1, the CRTM has undergone significant improvements, covering visible, infrared, and microwave sensors. For example, two computationally efficient radiative transfer solvers have been developed and are included within the CRTM: the advanced double-adding method (Liu and Weng 2006) and the successive-order-of-interaction method (Heidinger et al. 2006). Ding et al. (2011) emphasizes the importance of all-sky radiance assimilation to include an efficient and accurate radiative transfer forward model. In their study, the CRTM was assessed against not only reference radiative transfer models, but also satellite observations from the Atmospheric Infrared Sounder. Results showed that the CRTM performed well compared to the two different types of metrics.

Biases of infrared imagery for the Advanced Himawari Imager (Bessho et al. 2016) have recently been investigated in preparation for data assimilation (Zou et al. 2016). In their study, biases were between 0.6 and 1.2 K for all infrared channels, including imagery near $3.9 \mu m$. In addition, biases near $3.9 \mu m$ were found to show a dependence on satellite zenith angle over ocean scenes. Two radiative transfer models (CRTM and RTTOV) were used in their study; however, their analysis was confined to clear-sky scenes.

Over the past few decades, there has been steady progress toward all-sky satellite radiance assimilation at NCEP. To begin with, only clear-sky scenes were assimilated, to the current state of assimilating microwave radiances from nonprecipitating clouds over ocean-only scenes. To progress toward all-sky radiance assimilation of next-generation sensors like the *Geostationary Operational Environmental Satellite-16* (*GOES-16*) Advanced Baseline Imager (ABI; Schmit et al. 2017), and other types of future geostationary/polar-orbiting sensors, elimination of all possible errors that contribute to CRTM-generated imagery would be beneficial.

Work has already begun addressing all-sky radiance assimilation of *GOES-16* data. Zhang et al. (2016) used WRF-EnKF along with the CRTM in a "proof of concept" study that utilized observing system simulation experiments to study the impacts of assimilating all-sky radiances from *GOES-16*. In addition, Minamide and Zhang (2017) proposed a new flow-dependent adaptive observation error inflation method in a study to assimilate all-sky radiances from *GOES-16*.

Work in this paper addresses a weakness in calculated radiances by the CRTM for *GOES-12/13* brightness temperatures (Tbs) near $3.9 \mu m$ through the generation of imagery by the CRTM, which will be referred to as synthetic satellite imagery herein. Motivation for this study is in preparation of all-sky assimilation of imagery near $3.9 \mu m$ for future applications. Since water exists in three phases in the atmosphere of Earth, a distinction is made between water vapor, liquid water, and solid water herein. Tbs computed from the CRTM, version 2.1.3, near $3.9 \mu m$ were found to be inconsistent with observations for regions of solid-water clouds during the daytime. Since Tbs from the CRTM are used in the minimization process within data assimilation, accurate Tbs from the CRTM are essential for future all-sky assimilation of satellite data at these wavelengths at NCEP.

Seven sections are included in this paper. An introduction to the four case studies used herein is found in section 2. In preparation for the generation of synthetic imagery, information about the setup of the CRTM is provided in section 3. A direct comparison between synthetic and observed *GOES-12/13* imagery for all four cases is shown in section 4. Additional investigation into two of the cases, which includes discussions about the

TABLE 1. A summary of the date, time (UTC), NWP model, horizontal grid spacing (km), and microphysics of each case used for this study.

Date	Time (UTC)	Model	Horizontal grid spacing (km)	Microphysics
27 Jun 2005	2345	RAMS	2.0	RAMS
26 Jul 2013	0000	NSSL WRF-ARW	4.0	WSM6
29 Apr 2014	1800	CAPS WRF-ARW	4.0	Morrison
26 Aug 2014	1800	HWRF	2.0	Ferrier–Aligo

sensitivity of synthetic Tbs near both $3.9\,\mu$m and near $10.7\,\mu$m to the particle size of ice, is found in section 5. A brief consideration of NWP and CRTM errors is discussed in section 6. Both the summary and conclusions are discussed in the last section, section 7.

2. Four selected cases

Four cases have been chosen for this study that represent different simulated meteorological events, numerical models, and microphysics. To begin with, a convective case that occurred on 27 June 2005 over the High Plains of the United States was chosen. This case was characterized by different observed *GOES-12* reflective properties of anvils of thunderstorms near $3.9\,\mu$m (Grasso and Lindsey, 2011); in addition, the CSU-Regional Atmospheric Modeling System (RAMS) model and microphysics (Cotton et al. 2003) was used to simulate the event. A second case, used herein, was an unorganized convective event that occurred on 26 July 2013 over the United States, which was part of the daily real-time forecasts at the National Severe Storms Laboratory (NSSL); see Bikos et al. (2012) for additional details. Unlike the 27 June 2005 event, this case was characterized by Advanced Research WRF (WRF-ARW; Skamarock et al. 2005) simulated anvil canopies, with the WSM6 microphysics, that were too small in areal extent when compared to their observed counterparts in *GOES-13* imagery. Improvements were accomplished with modifications in the original WSM6 scheme in the study; see Grasso et al. (2014) for additional details and references.

Since the third case has yet to be published, additional details are provided presently. As part of the GOES-R Proving Ground (Goodman et al. 2012) and the Hazardous Weather Testbed (Clark et al. 2012) programs, output from WRF-ARW using different microphysical options were evaluated; for a recent example see Thompson et al. (2016). Output from several configurations of WRF-ARW was provided by the Center for the Analysis and Prediction of Storms (CAPS) in a domain that covers the United States with 4-km horizontal grid spacing (Kong et al. 2007; Xue et al. 2007). Model data from an 18-h forecast valid at 1800 UTC 29 April 2014 for a WRF-ARW

simulation of a conspicuous extratropical low pressure system that used the Morrison microphysics (Morrison and Pinto 2005, 2006) were acquired from CAPS for use in this study. Last, a tropical cyclone event was chosen for the fourth case: Hurricane Cristobal, which was over the western Atlantic on 26 August 2014. Observations of hurricane Cristobal were part of an all-sky radiance assimilation study that employed the operational HWRF system along with the operational Ferrier–Aligo microphysics; see Wu et al. (2018) for further details and references. A brief summary of the four cases is displayed in Table 1.

3. CRTM_2.1.3 setup

To create synthetic imagery, output from each of the above simulated events was passed to the CRTM (version 2.1.3). Simulated output from numerical weather prediction (NWP) models consisted of the following three-dimensional variables: pressure, temperature, water vapor mixing ratio, along with the mass mixing ratio and the diagnosed particle size of cloud water, rainwater, graupel, snow, and ice. Further, the following two-dimensional fields were passed to the CRTM: latitude, longitude, canopy or skin temperature, and monthly averaged surface spectral emissivity (Seemann et al. 2008). Unluckily, the linking of model-simulated output, particularly the microphysics, with the CRTM likely creates a lack of compatibility between simulated model variables and expected input variables by the CRTM.

Since numerical weather prediction (NWP) microphysical schemes and the CRTM are developed independently of one another, there exists the unforeseen potential for inconsistencies to occur between characteristics of microphysical species that are simulated by NWP models and characteristics of microphysical species assumed by the CRTM. For example, RAMS predicts two moments for the following eight habit types: small cloud droplets, large cloud droplets, rainwater, snow, graupel, hail, aggregates, and pristine ice, while the CRTM carries five (six) habit types: cloud water, rainwater, graupel, snow, and ice (hail). To include all simulated habits, small and large cloud droplets were combined to the CRTM's cloud water category followed

by the accumulation of graupel, snow, and aggregates to the CRTM's snow category while hail became the CRTM's graupel habit. Depending on the wavelength—infrared versus microwave—of the synthetic image, some habit types may be neglected or must be included. Although the particle size distribution may be similar in formulation in a wide range of microphysical schemes, one can make changes to simulated habits that may be inconsistent with those of the CRTM. Habit geometry and density of simulated species can also differ from what is assumed by the CRTM. For example, ice density is different between many microphysical schemes—both the Morrison (Reisner et al. 1998; Morrison et al. 2009) and Milbrandt and Yau (Milbrandt and Yau 2005) use $500.0 \, \text{kg m}^{-3}$, Thompson (Thompson et al. 2004) uses $890.0 \, \text{kg m}^{-3}$, and the Morrison and Milbrandt P3 scheme (Morrison and Milbrandt 2015) suggest $916.0 \, \text{kg m}^{-3}$ while the CRTM uses $900.0 \, \text{kg m}^{-3}$. Ice geometry is assumed spherical by many microphysical schemes, but not all. The Milbrandt and Yau scheme uses a value of $\alpha = 440$ to approximate the geometry of bullet rosettes in the mass power-law formulation for ice. As a concluding example, changes in the dispersion parameter of the size distribution can be made during a simulation that may be inconsistent with values used by the CRTM. Milbrandt and Yau use a dispersion value of 3.0 for ice while Morrison uses a value of 0.0. Inconsistencies develop since optical properties used by the CRTM are computed from one fixed set of microphysical characteristics. Further, the use of effective radius or diameter, also used by the CRTM, may be inconsistent at some wavelengths. As a result, Sieron et al. (2017, 2018) have suggested a solution that can remove inconsistencies between simulated microphysics and assumed microphysics in the CRTM: users would build their own microphysics specific optical tables to replace the default table embedded within the CRTM.

There is an additional issue related to NWP microphysics and radiative transfer models. An area of active research is to address inconsistencies between 1) how NWP microphysics interacts with an internal NWP radiation scheme and 2) how an NWP microphysics interacts with an external, stand-alone, radiative transfer model scheme. Additional information about potential inconsistencies between NWP microphysics and radiative transfer models can be found in Senf and Deneke (2017) along with references therein.

In addition to microphysical compatibility between NWP models and the CRTM, two aspects within the CRTM itself improved in this study and are noted. First, a coding error that caused the neglect of solar reflection was corrected. Synthetic imagery generated from the CRTM with the error is referred to as "ada_error."

Likewise, synthetic imagery generated from the CRTM with the error fixed is referred to as "ada_fixed." Inclusion of solar reflection has been added to the publicly released CRTM, version 2.3.0, on 27 November 2017. Second, CRTM's ice optical property lookup table (LUT) was updated. To deal with multiple scattering phase functions, the delta-fit method (Hu et al. 2000) was used by CRTM. Further, the CRTM was run using a six-stream zenith-angle resolution. A discovery was made that the delta-fit coefficients used by CRTM's optical property LUT were erroneously calculated for ice. An example of a set of six-stream delta-fit coefficients, from CloudCoeff.bin, version 3.04 (embedded in the CRTM), for imagery near $3.9 \, \mu\text{m}$ and an ice particle having an effective radius of $16.53 \, \mu\text{m}$ that resulted from a quadratic interpolation in four wavelengths and four effective radii were -2.1417×10^{-2}, -3.5695×10^{-2}, -3.6044×10^{-2}, -9.8545×10^{-2}, -9.9924×10^{-2}, and 1.4059×10^{-2}. An updated CloudCoeff.bin, version 3.07, was provided by the CRTM team that contained correct values. The updated set of delta-fit coefficients of an ice particle with the same effective radius as above became 0.8404, 0.9043, 0.7250, 0.4775, 0.1765, and 0.7054. As a result, the coefficients were corrected and the ice particle database was updated to include the latest improvements (Yang et al. 2013; Baum et al. 2014). Synthetic imagery generated with the erroneous LUT is referred to as "cloudcoeff_3.04" and with the updated LUT as "cloudcoeff_3.07." The numbers 3.04 and 3.07 refer to the version of the optical properties in the CRTM LUT. As of this writing, the inclusion of the updated LUT into the publicly released CRTM is unknown.

4. Results: Observed and synthetic imagery

Imagery near $3.9 \, \mu\text{m}$ from the four cases discussed in section 2 is presented in this section. A four-paneled figure will be shown below for each case, which contains observed imagery and three synthetic images from the CRTM, version 2.1.3. As discussed in section 3, two errors were found and resolved in the version of the CRTM used for this study. As a result, the following three different images from the CRTM are each presented with two labels: 1) ada_error and cloudcoeff_3.04, 2) ada_fixed and cloudcoeff_3.04, and 3) ada_fixed and cloudcoeff_3.07. Side-by-side placement of imagery, for a given case, allows for a direct comparison of the impact of each error, on the imagery from the CRTM, with observations.

Brightness temperatures of convective anvils near $3.9 \, \mu\text{m}$ were different in observations and simulation on 27 June 2005. In particular, observed *GOES-12* Tbs near $3.9 \, \mu\text{m}$ were approximately 20 K greater, in general, for
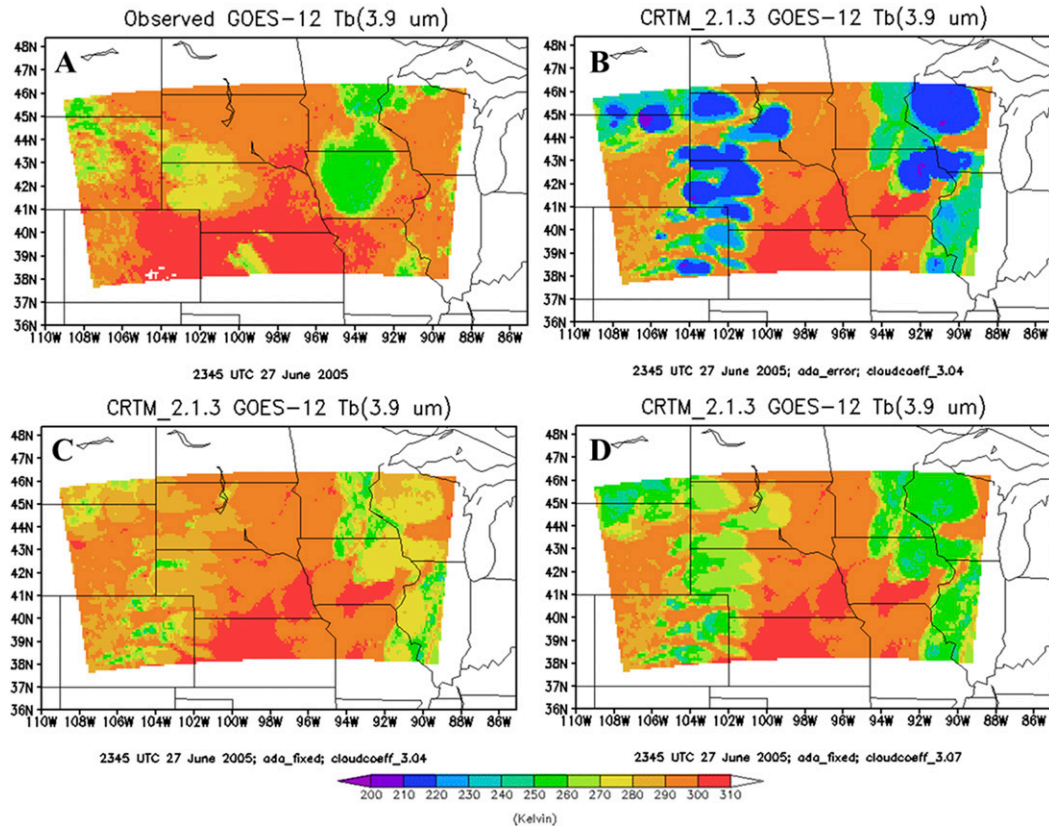
FIG. 1. Remapped *GOES-12* Tbs (K) near 3.9 μm valid at 2345 UTC 27 Jun 2005 from (a) observations and from the CRTM_2.1.3 with (b) ada_error and cloudcoeff_3.04, (c) ada_fixed and cloudcoeff_3.04, and (d) ada_fixed and cloudcoeff_3.07. Values of observed Tbs of anvils in (a) over western Nebraska were greater than those over Iowa. This characteristic was also evident in the synthetic image (d) when both CRTM errors were corrected.

convective anvils over western Nebraska compared to those over Iowa (Fig. 1a). Synthetic imagery originally developed for this case was used to identify and fix an error in the prediction of pristine ice number concentrations in the microphysics within RAMS (Grasso and Lindsey 2011). Imagery from the CRTM generated with ada_error and cloudcoeff_3.04 exhibited *GOES-12* Tbs near 3.9 μm (Fig. 1b) of convective anvils that were approximately 40 K less than observations (Fig. 1a). After solar reflection was activated and the CRTM rerun with ada_fixed and cloudcoeff_3.04, Tbs near 3.9 μm of the simulated convective anvils increased nearly 60 K (Fig. 1c) compared to those in Fig. 1b and about 10–20 K greater than observations (Fig. 1a). Although Tbs of the observed anvils over western Nebraska were greater than those over Iowa, results from the CRTM (Fig. 1c) lack the observed temperatures difference between simulated anvils in the two respective regions. When the CRTM was run with ada_fixed and cloudcoeff_3.07, not only did Tbs of anvils decrease, but also indications of slightly greater values of Tbs of convective anvils over

western Nebraska compared to those over Iowa became evident (Fig. 1d). Another way to quantify the impact of the two CRTM errors—solar reflection and optical properties—is through the use of histograms of synthetic imagery.

Histograms of imagery in Figs. 1a and 1b are displayed in Fig. 2a within which a local peak of observed Tbs for observed anvils was near 255 K while the corresponding peak for simulated anvils was near 215 K. Values of the mean absolute error (MAE) and bias were approximately 14 and −11 K, respectively. Inspection of the histograms from observations and the CRTM (Fig. 2a) suggests that values of the cold bias and MAE were a consequence of the 40-K shift of the simulated peak near 215 K away from the observed peak near 255 K. Although the bias increased to about −1 K and the MAE decreased to near 6 K when solar reflection was activated, the location of the simulated peak near 215 K (Fig. 2a) shifted to near 280 K (Fig. 2b), about 20 K greater than the location of the observed peak. With both CRTM errors corrected, the location of the
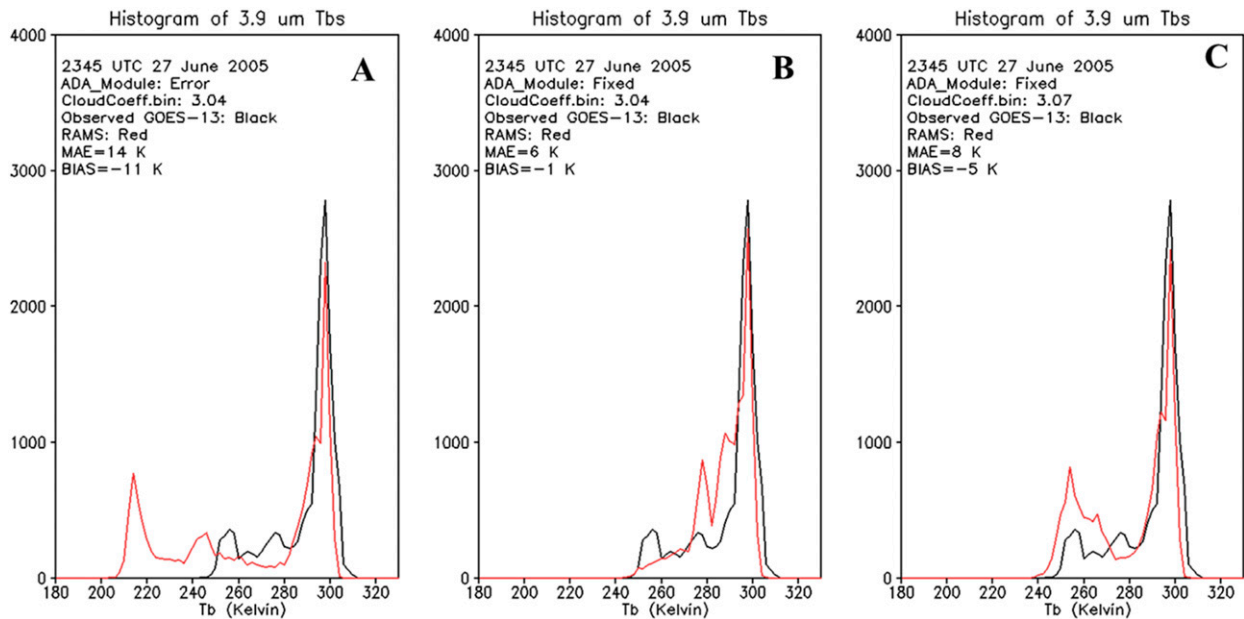
FIG. 2. Histograms, in 2-K bins, of observed (black) and CRTM_2.1.3 (red) *GOES-12* Tbs near 3.9 μm valid at 2345 UTC 27 Jun 2005 from Fig. 1. CRTM Tbs were computed using (a) ada_error and cloudcoeff_3.04, (b) ada_fixed and cloudcoeff_3.04, and (c) ada_fixed and cloudcoeff_3.07. Mean absolute errors and biases are included in each panel. In particular, the RAMS model and microphysics were used for this case.

simulated peak decreased close to observed values near 255 K (Fig. 2c). Although the temperature of the simulated peak was near the observed peak, the amplitude of the simulated peak, approximately 800 points, was greater than observations, approximately 400 points, and was also reflected in the values of the bias and MAE. A comparison of Figs. 1a and 1d indicated that the RAMS simulation produced more convective anvils than observed and can explain the greater amplitude of the simulated peak compared to the observed peak near 255 K in the histograms in Fig. 2c.

Synthetic imagery has been used to aid in the identification of model errors associated with the size of anvil canopies of convective storms. Output for the second case, 25 July 2013, was generated from NSSL WRF-ARW using the WSM6 microphysics. One of the main features of output for this case was the consistent occurrence of simulated anvil canopies that were smaller than observed anvil canopies (Grasso et al. 2014). Observed *GOES-13* Tbs near 3.9 μm of anvil canopies were approximately 250 K over the continental United States (Fig. 3a). In sharp contrast, CRTM *GOES-13* imagery with ada_error and cloudcoeff_3.04 exhibited Tbs near 215 K for simulated anvils (Fig. 3b). When the CRTM was rerun with ada_fixed and cloudcoeff_3.04, anvil Tbs increased to near 260 K (Fig. 3c), a trend that was similar to the 27 June 2005 case just presented. However, there was one exception: Tbs of the solid-water cold clouds of

the convection east of the eastern seaboard of the United States (Fig. 3c) remained similar to those of Fig. 3b. At 0000 UCT 26 July 2013 there was no solar reflection over the western Atlantic since the day/night terminator was located nearly coincident with the East Coast of the United States. A comparison of Tbs of anvils over the central plains in Fig. 3c with those in Fig. 3a suggested that values of Tbs of anvil canopies were slightly greater than observations. Tbs decreased, however, when the CRTM was rerun with ada_fixed and cloudcoeff_3.07 (Fig. 3d).

Histograms for the second case were also generated as another means to highlight the impact of the two CRTM errors on synthetic imagery. A comparison between observed and synthetic imagery for the 26 July 2013 case shows peaks near 255 and 235 K for observed/synthetic Tbs of anvils, respectively (Fig. 4a). Similar to the first case, a shift of the peak of Tbs of solid-water cloud tops from 235 to near 275 K occurred with ada_fixed and cloudcoeff_3.04 (Fig. 4b). Unlike the first case, a rather low amplitude peak remained near 235 K (Fig. 4b). As a reminder, the lack of solar reflection over the western Atlantic resulted in values of Tbs that were less for anvil canopies compared to regions over the United States (cf. Figs. 3b and 3c). Also evident was an increase in the amplitude of the peak near 300 K in Fig. 4b. This result was the consequence of solar reflection from low-level clouds over the eastern Pacific in Fig. 3c, which was
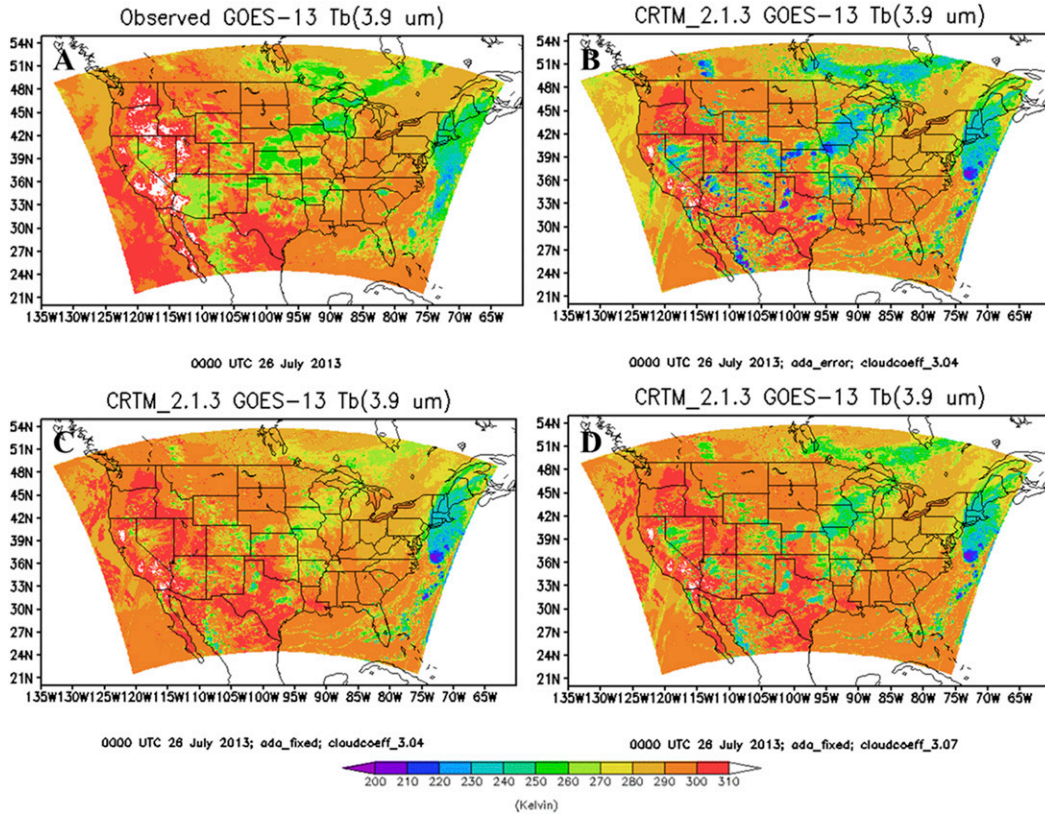
FIG. 3. As in Fig. 1, but with remapped *GOES-13* Tbs (K) near 3.9 μm valid at 0000 UTC 26 Jul 2013.

absent in Fig. 3b. As a result of the inclusion of solar reflection, values of the bias increased from −4 K, a cold bias, to +1 K, a warm bias, while values of the MAE decreased from 8 to 6 K. Inspection of the histograms in

Fig. 4b shows that values of Tbs for the simulated solid-water cold cloud tops exceeded observations by approximately 20 K. After the inclusion of the new LUT, cloudcoeff_3.07, the location of the peak in values of
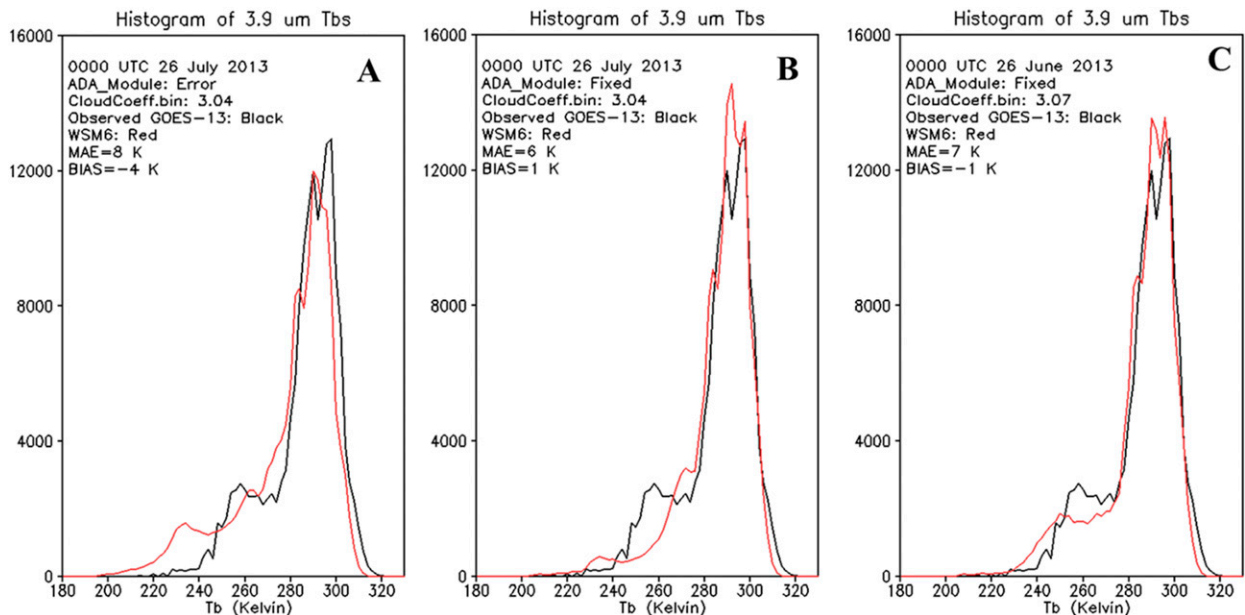
FIG. 4. As in Fig. 2, but using remapped data shown in Fig. 3. Further, the NSSL WRF-ARW with the WSM6 microphysics was used for this case.
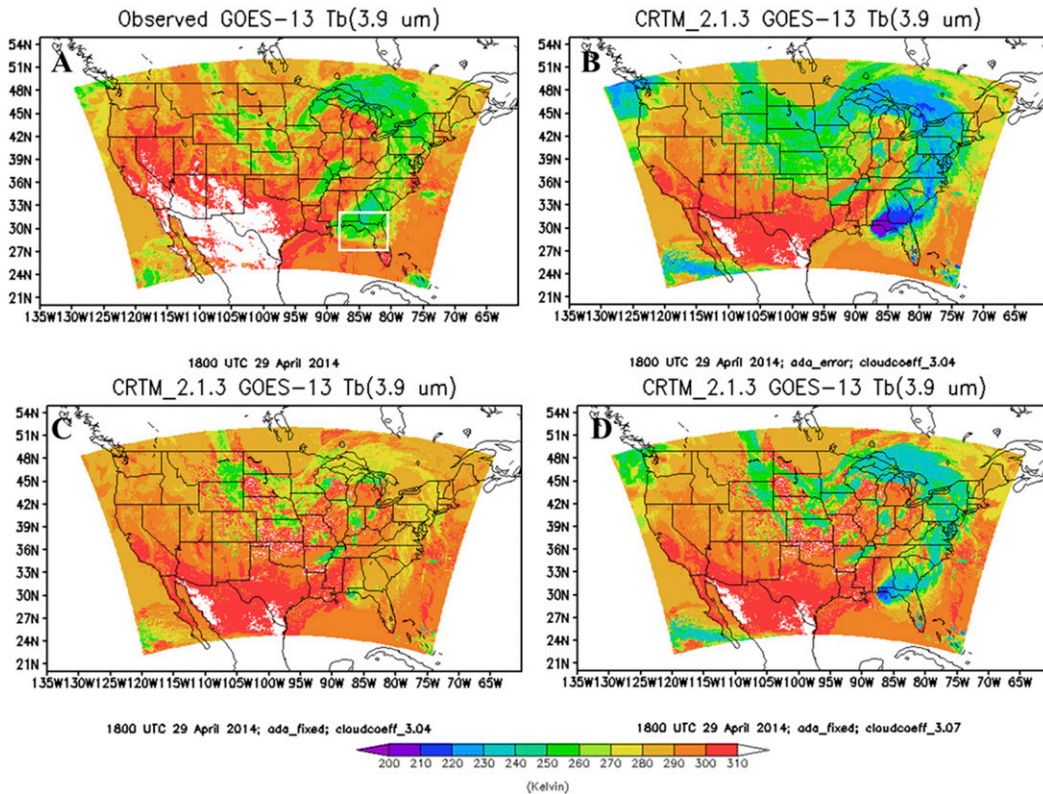
FIG. 5. As in Fig. 1, but with remapped *GOES-13* Tbs (K) near 3.9 μm valid at 1800 UTC 29 Apr 2014. The white box over northern Florida in (a) shows the region of a MODIS image that is displayed in Fig. 9.

simulated Tbs for anvil canopies decreased to near 250 K, slightly below observations. In response to the cooler shift in synthetic Tbs, values of the bias decreased to −1 K while the MAE increased slightly to 7 K. There was one common behavior that both the 27 June 2005 and this case shared: with a lack of solar reflection and with the use of the original LUT, synthetic Tbs of anvil canopies were a few tens of kelvins less than observations. When solar reflection was activated and the original LUT was used, synthetic Tbs of solid-water cloud tops increased above observations. Only after the inclusion of both solar reflection and the new LUT did simulated Tbs of anvil canopies decrease to near observed values.

An extratropical low pressure system was the primary weather event over the continental United States in the third case, which occurred on 29 April 2014. As a reminder, this case was simulated with WRF-ARW along with the Morrison microphysics. Similar to the previous two cases, a visual comparison between observed and synthetic *GOES-13* Tbs near 3.9 μm (Figs. 5a and 5b) illustrated that values of Tbs of synthetic cold cloud tops were less than observations by approximately 25 K. When solar reflection was activated in the CRTM,

resulting values of Tbs of cold cloud top increased beyond observations. In particular, values of synthetic Tbs exceeded observations associated with the cloud field from the Great Lakes region, southward along eastern portions of the United States to western portions of the Florida Panhandle (Fig. 5c). Also note the increase in Tbs associated with low-level clouds over South Dakota southward to Oklahoma then northeastward to Illinois. When the new LUT was included, CRTM Tbs decreased for the solid-water cold clouds associated with the extratropical low pressure system (Fig. 5d). However, little change was evident for the values of Tbs associated with the low-level clouds when comparing Figs. 5c and 5d. This result was to be expected since the new LUT contains corrected optical properties only for ice.

Histograms are also presented for the 29 April 2014 case as a way to further evaluate the impact of both CRTM errors on synthetic imagery. With a lack of solar reflection, value of Tbs were nearly 20 K less for the peak of synthetic imagery associated with solid-water cold cloud tops compared to the observed peak of ice clouds that was near 250 K (Fig. 6a). As a result of the cold shift of the histogram of synthetic Tbs, values of the bias were nearly −8 K along with a MAE of 10 K. There
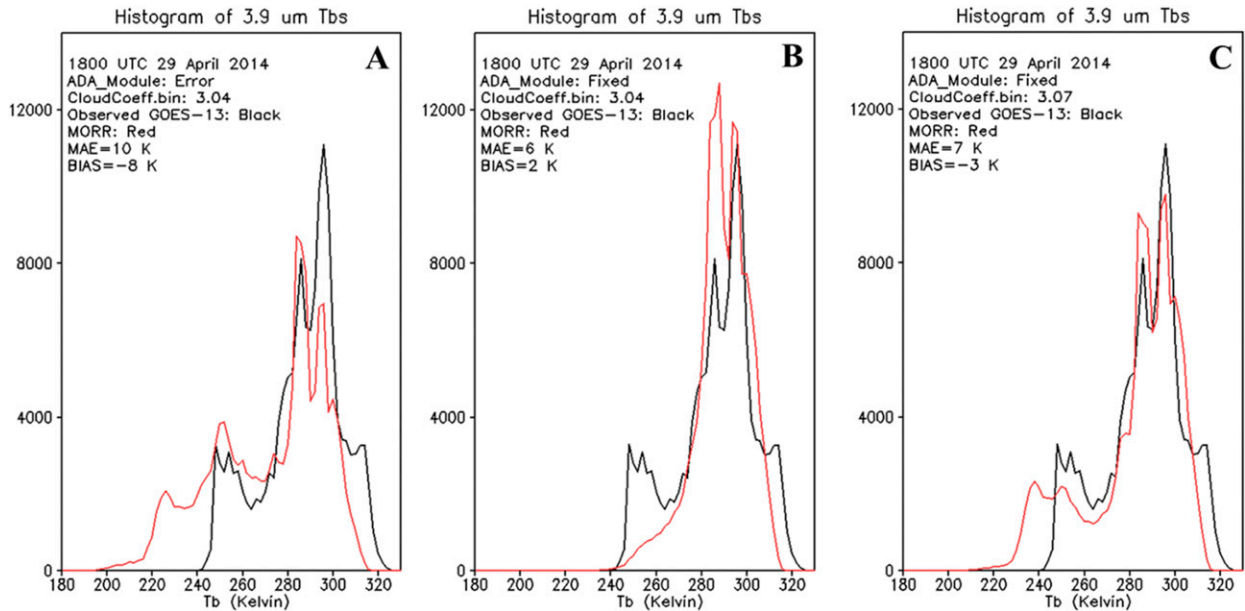
FIG. 6. As in Fig. 2, but using remapped data shown in Fig. 5. This case was simulated with WRF-ARW along with the Morrison microphysics.

were two primary changes in the synthetic histogram when solar reflection was activated (Fig. 6b): 1) an approximate 45-K warming occurred associated with solid-water cold cloud tops and 2) an approximate 30-K warming associated with low-level clouds from 250 to near 290 K. That is, the peak near 230 K in Fig. 6a was associated with high clouds and the second peak near 250 K in Fig. 6a was associated with the low-level clouds in Fig. 5c. In accord with the increased values of Tbs, values of the bias increased to 2 K while the value of the MAE decreased to approximately 6 K. Values of synthetic Tbs of the high clouds decreased with the inclusion of the new LUT to near 240 K, about 10 K less than observations (Fig. 6c). Because of the reduction of values of synthetic Tbs, the value of the bias also decreased to −3 K, which indicated a cold bias of synthetic imagery compared to observations.

As stated in the introduction, motivation for this study is in preparation for all-sky radiance assimilation in an operational environment. Therefore, the fourth case presented herein is a tropical system, Hurricane Cristobal, which was over the western Atlantic on 26 August 2014. This weather event was part of an all-sky radiance assimilation study using NCEP's operational HWRF system Wu et al. (2018). The operational HWRF system included GSI and version 2.2.3 of the CRTM. In keeping with presenting cases generated with different microphysical schemes, the operational Ferrier–Aligo microphysics was used for the simulation of Cristobal.

Once the HWRF-simulated total condensate mass field was partitioned into distinct species, the CRTM herein was used to generate synthetic imagery. Total condensate was partitioned into distinct species by using the prognostic total condensate field and ice fraction to generate liquid-water and solid-water condensate fields. Liquid water was partitioned into rain and cloud using a rain fraction variable while the prognostic riming rates were used to generate the other solid-water species. A direct comparison of observed and synthetic GOES-13 Tbs near 3.9 µm is shown in Figs. 7a and 7b. Both figures suggest that without solar reflection, values of synthetic Tbs were generally 40 K less than observations for cold cloud tops. When the CRTM was rerun with ada_fixed and cloudcoeff_3.04, synthetic Tbs appeared to increase only slightly for the cold cloud tops. This result is in sharp contrast to the past three cases discussed above; that is, when solar reflection was activated, values of synthetic Tbs of solid-water clouds generally increased to values that exceeded observed values in the other cases. However, similar to the above three cases, when the new LUT was included along with solar reflection, values of synthetic Tbs decreased.

Histogram plots for the 26 August 2014 case (Fig. 8) also highlight the unique behavior of the values of synthetic Tbs when solar reflection and the updated LUT were included. Histogram peaks associated with the cold clouds indicated that observed (synthetic) values of Tbs near 3.9 µm were approximately 250 (225) K (Fig. 8a). Inspection of Fig. 8a exhibits a noticeable shift of the
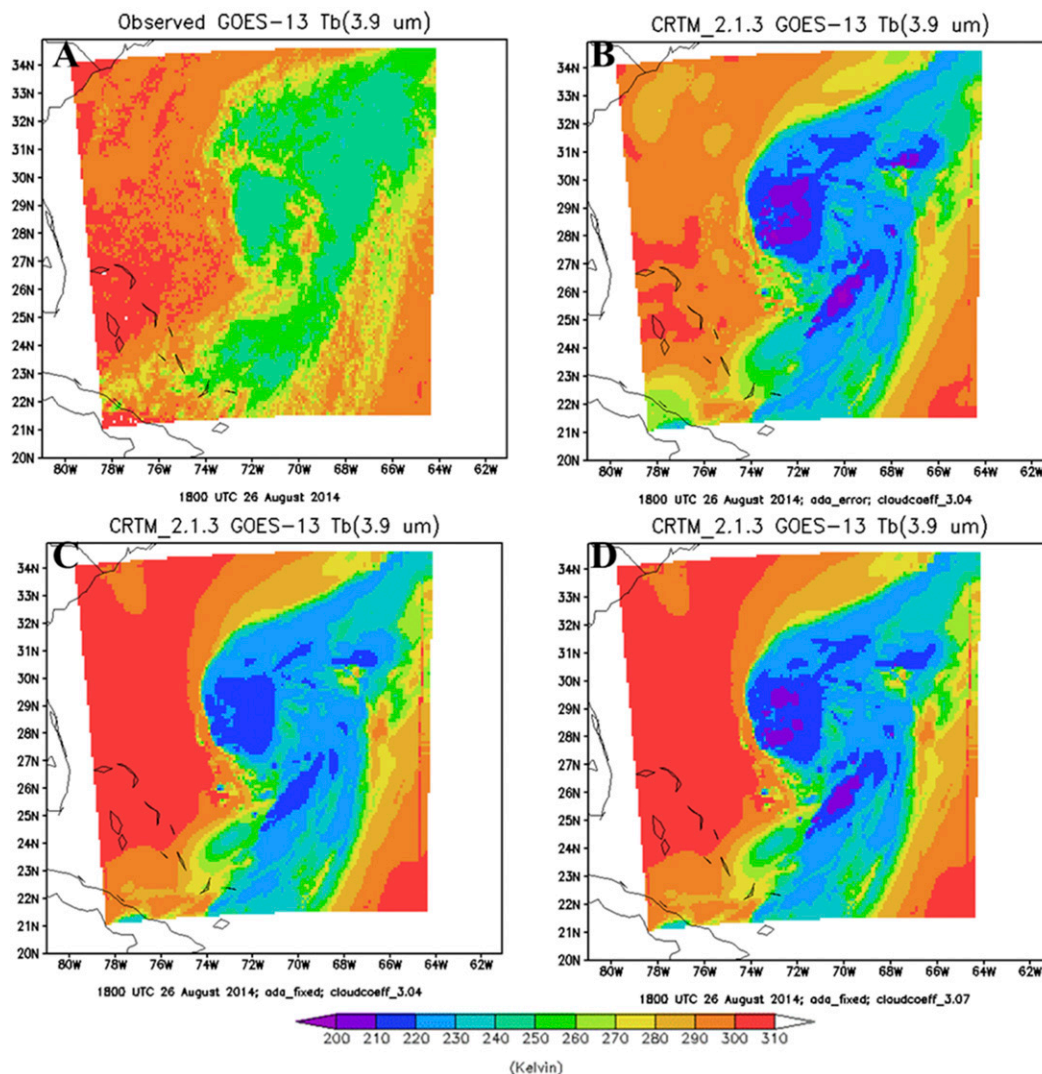
FIG. 7. As in Fig. 1, but with remapped *GOES-13* Tbs (K) near 3.9 μm valid at 1800 UTC 26 Aug 2014.

synthetic histogram toward colder temperatures relative to the observed histogram, which resulted in values of the bias and MAE of -9 and 11 K, respectively. When solar reflection was included, only a slight change of the synthetic histogram was evident near 225 K (cf. Figs. 8a and 8b). Similar to the previous two cases, 26 July 2013 and 29 April 2014, the amplitude of the synthetic histogram near 300 K increased significantly (Fig. 8b) because of the increased values of synthetic Tbs located to the west of Cristobal (cf. Figs. 7b and 7c). Although the pattern of the cold peak near 225 K changed little, values of the bias (MEA) increased (decreased) to approximately -6 (10) K in response to the increased amplitude of the synthetic peak near 300 K. With the inclusion of the new LUT, changes in the resulting synthetic histogram, although present, were difficult to

visually identify (cf. Figs. 8b and 8c). Values of both the bias and MAE also remained essentially the same at -6 and 10 K, respectively.

5. Additional study of the 29 April 2014 and 26 August 2014 cases

Since additional details of the first two cases appear in the literature, further study of the last two cases is presented in this section. As a reminder, after both solar reflection and the new LUT were used to generate synthetic imagery near 3.9 μm for the 29 April 2014 case, the location of the peak associated with cold cloud tops of the synthetic histogram shifted toward colder temperatures when compared to observations (Fig. 6c). As was shown in Grasso and Lindsey (2011) for the 27 June
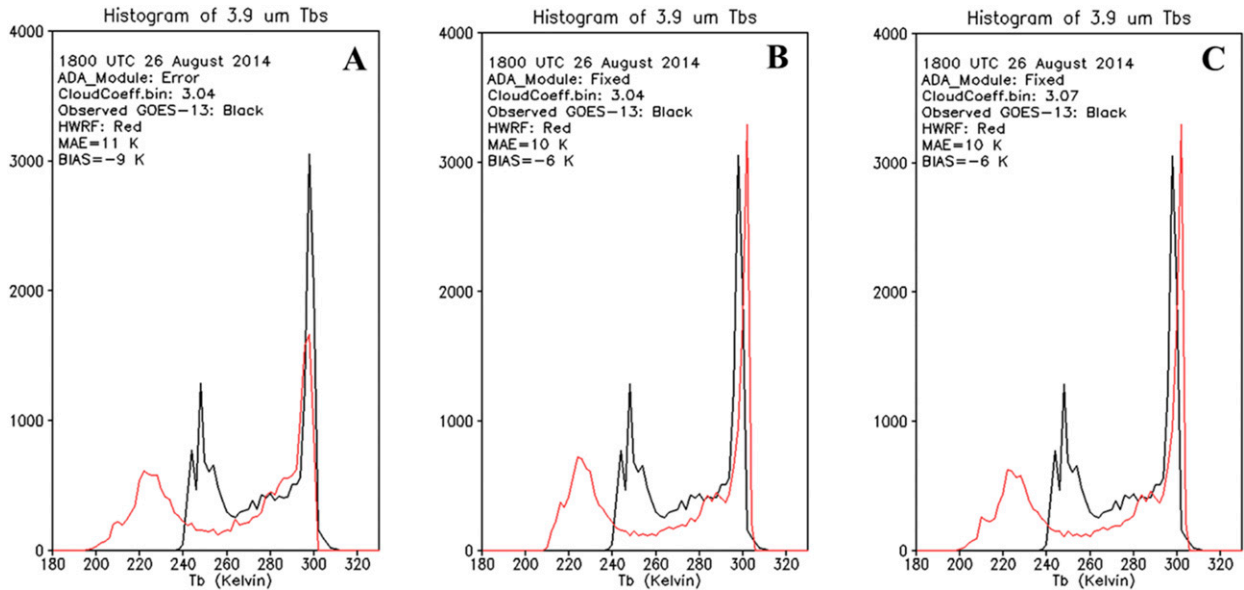
FIG. 8. As in Fig. 2, but using remapped data shown in Fig. 7. Unlike the other three cases, the operational HWRF system, which used the Ferrier–Aligo microphysics, was used for this case.

2005 case, values of synthetic Tbs near $3.9\,\mu m$ were sensitive to the size of ice particles when solar reflection was present. Specifically, values of the mass extinction and single-scattering albedo are inversely proportional to particle size of ice when the particle radius is less than approximately $50\,\mu m$. As a result, there exists the potential for values of the synthetic Tbs near $3.9\,\mu m$ in Fig. 5d to increase by reducing the size of ice. Observations were used as guidance to demonstrate the potential impact of ice particle size on values of synthetic Tbs near $3.9\,\mu m$. Values of effective radii (μm; collection-6 level-2 data) from the *Aqua* Moderate Resolution Imaging Spectroradiometer (MODIS), valid at 1845 UTC 29 April 2014, are shown in Fig. 9. A constant value was chosen to recompute synthetic imagery because of some limitations of the MODIS-retrieved effective radii; such as, but not limited to the following: 1) the spatial mismatch between MODIS and simulated cloud fields, 2) incomplete coverage of MODIS data with the domain of synthetic imagery, and 3) the choice of three simulated frozen habits—ice, snow, and graupel—and only one retrieved frozen effective radii. A comparison of values of Tbs in Figs. 5a and 5c indicated that the values of Tbs associated with convection adjacent to and south of the Florida Panhandle were less than observations. As a result, an effective radius of $25\,\mu m$, from Fig. 9, was used for ice in a subsequent CRTM generated image near $3.9\,\mu m$. After using the same configuration as in Fig. 5d, values of synthetic Tbs increased (cf. Figs. 10a and 5a and 5d). A histogram plot of TBs in Fig. 10a demonstrated a

warm shift of the original location of the peak near 240 K (Fig. 6c) to near observed values of approximately 250 K (Fig. 10b). However, similar to the enhanced amplitude of the cold peak near 250 K in Fig. 2c for the 27 June 2005 case, the amplitude of the peak near 250 K in Fig. 10b suggested that WRF-ARW produced too many
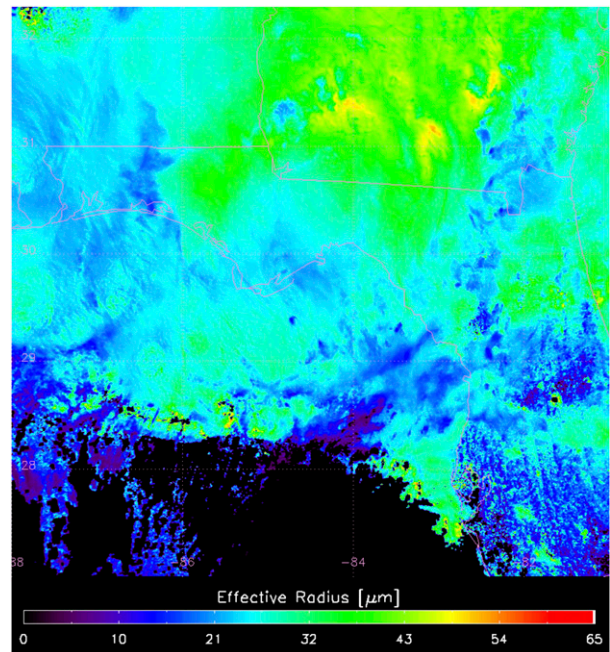

FIG. 9. Enhanced image showing MODIS cloud particle effective radius (μm) valid at 1845 UTC 29 Apr 2014.
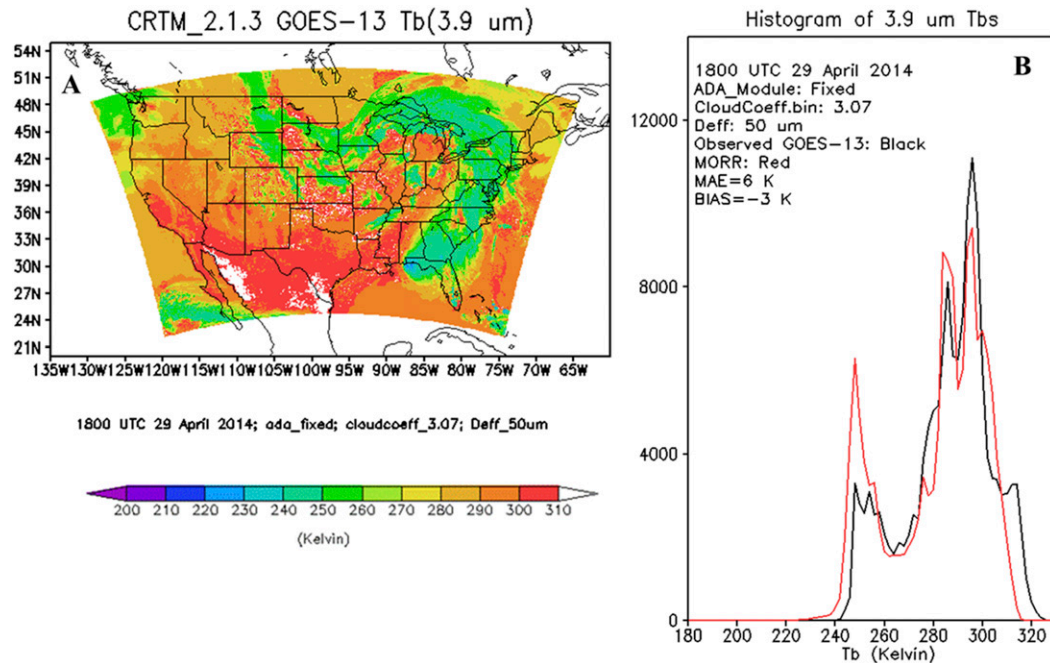
FIG. 10. (a) As in Fig. 5d, but with the effective diameter (Deff) = 50 μm for ice. (b) As in Fig. 6c, but with Deff = 50 μm for ice.

cold clouds, compared to observations, for the 29 April 2014 case. Despite the 10-K warm shift and a small decrease in the MAE to 6 K, values of the bias remained essentially unchanged at −3 K; possibly because of the existence of additional cold clouds in the simulation. Thus far, all synthetic imagery has been produced near 3.9 μm. As a result, one may wonder about the impact of ice particle size on values of Tbs at other wavelengths.

Synthetic imagery was produced only for one infrared wavelength for the 29 April 2014 case. Consequently, results are unable to be generalized to all other possible infrared wavelengths. Remapped observed *GOES-13* imagery near 10.7 μm is shown in Fig. 11a along with synthetic imagery at the same wavelength in Fig. 11b. Values of observed Tbs support values of synthetic Tbs save for the larger region of synthetic Tbs near 210 K over southern Georgia toward the western Florida Panhandle associated with deep convection. When an effective diameter of 50 μm was used for the size of simulated ice, values of the resulting Tbs exhibit a slight cooling for the cold cloud tops (Fig. 11c). A few features associated with the imagery were also evident in plots of histograms in Fig. 11d. Although the peak in each synthetic image near 290 K was similar in temperature to the observed peak, the amplitude of each synthetic plot was larger than observations. Inspection of each synthetic image with the observed images suggested that surface temperatures simulated by WRF-ARW, with

the Morrison cloud microphysics, over Texas, westward over New Mexico, Arizona, and Nevada were too low compared to observations. A second region where the peaks of the synthetic imagery differed from the observed peak was near 260 K in Fig. 11d. This difference may be explained by a lack of simulated midlevel clouds in and around the High Plains of the United States. A third region where there was a difference between the synthetic and observed peaks was near 220 K. Values of Tbs with an effective diameter of 50 μm resulted in slightly cooler cloud tops associated with convection over the southeast. Although values of the MAE were approximately 6 K for each synthetic image, there was a decrease in the bias from −1 to −2 K when the particle size was changed.

Sensitivity of the values of Tbs to particle size of ice was also conducted for the tropical system that occurred on 26 August 2014. Based on satellite measurements of particles sizes (derived from *Terra* MODIS) in Fig. 12, a value of the effective diameter of 75 μm was used to generate imagery. Unlike particle sizes in the other three microphysical packages, the effective diameter of ice in the Ferrier–Aligo is simply set to a constant value of 150 μm. Thus, the size of ice was reduced by a factor of 2.0 based on observations. Despite the reduction of ice sizes, little if any change was evident in the new image near 3.9 μm, Fig. 13a, when compared to the image in Fig. 7c. Although less obvious in the histograms (cf. Figs. 8c and 13b), a slight cooling occurred, which
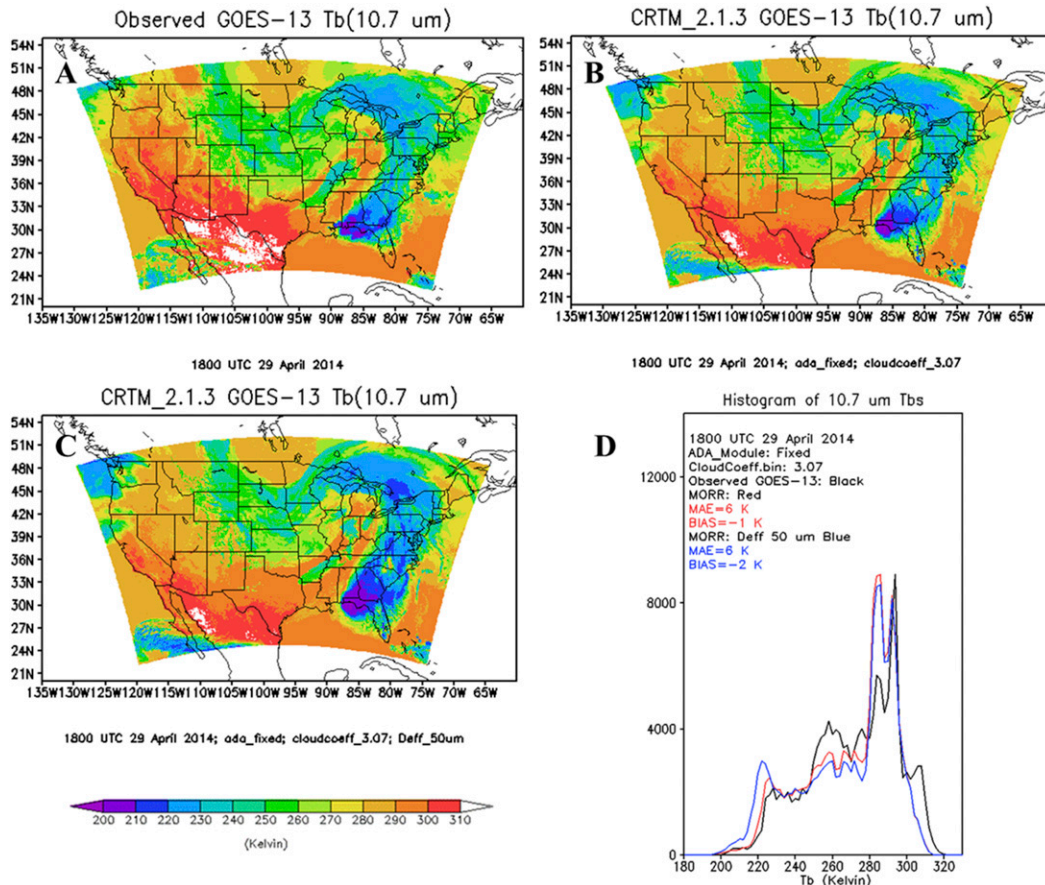
FIG. 11. Remapped *GOES-13* Tbs (K) near 10.7 μm valid at 1800 UTC 29 Apr 2014 from (a) observations, and from the CRTM_2.1.3 with (b) ada_fixed and cloudcoeff_3.07 and (c) ada_fixed, cloudcoeff_3.07 and Deff = 50 μm. (d) Histograms, in 2-K bins, of observed (black) and CRTM_2.1.3 with ada_fixed and cloudcoeff_3.07 (red) and with ada_fixed, cloudcoeff_3.07, and Deff = 50 μm (blue).

resulted in a decrease in the value of the bias from -6 (Fig. 8c) to -8 K (Fig. 13b) while the MAE remained the same at 10 K. Similar to the 29 April 2014 case, the sensitivity of Tbs to ice particle size was explored at one infrared wavelength.

Similar to the 29 April 2014 case, synthetic imagery was produced at 10.7 μm. A direct comparison of observed and synthetic *GOES-13* 10.7-μm Tbs is shown in Figs. 14a and 14b. As is evident, HWRF produced a cold cloud shield that exceeded the areal expanse of the observed cold cloud shield. After the effective diameter of ice was reduced to 75 μm, little if any change occurred in the synthetic image (cf. Figs. 14b and 14c). Histogram plots in Fig. 14d highlight both 1) the cold bias of the synthetic imagery with a bias of -5 K and a MAE of 8 K for each synthetic image and 2) the histograms of each synthetic image are nearly identical. That is, synthetic imagery at 10.7 μm remained essentially unchanged with a reduction of ice effective diameter.

6. NWP and CRTM errors

Although the focus of this study is errors associated with the CRTM, version 2.1.3, errors associated with simulated microphysics was also suggested. In particular, values of Tbs near 3.9 μm of (i) convective tops over the western Florida Panhandle (cf. Figs. 5a and 5d) and (ii) convective tops of Cristobal (cf. Figs. 7a and 7b–d) remained noticeably colder than observations despite the solar and LUT corrections in the CRTM. Preliminary examination of the 29 April and 26 August 2014 suggested that values of the ice mass mixing ratio are too small at the tops of the convective systems. Both snow and graupel represent habit categories with particle sizes large enough that little reflection of solar energy near 3.9 μm occurs relative to that of ice. Since the hypothesis is that the ice mass is too small, this implies that values of the optical depth are also too small. As a consequence, the ice fields offers less interference—because of relatively
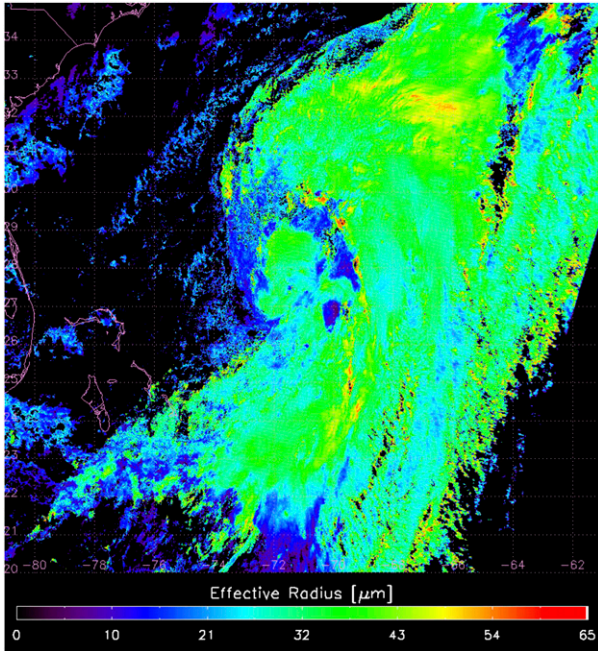
FIG. 12. Enhanced image showing MODIS cloud particle effective radius (μm) valid at 1540 UTC 26 Aug 2014.

low values of optical depth—and reflection to solar energy at 3.9 μm compared to the larger particles of the snow and graupel habit types near the tops of simulated convective clouds. A series of sensitivity experiments have yielded

positive results by modifying the ice mass mixing ratio field. In an attempt to maintain brevity; however, additional details into these matters are reserved for future work.

7. Summary and conclusions

Cold solid-water cloud-top Tbs near 3.9 μm computed from the CRTM, version 2.1.3, departed significantly from observed values. Synthetic imagery was generated using output from four different models, different microphysics, and different meteorological events: RAMS with the two-moment microphysics and variable reflective anvils; NSSL WRF using the WSM6 microphysics for unorganized warm season convection; WRF-ARW with the Morrison microphysics for an extratropical low; and the operational HWRF, which uses the Ferrier–Aligo microphysics for a tropical system. Values of Tbs of imagery near 3.9 μm from the CRTM were approximately 30 K less than observed values. Regions of the discrepancy were associated with solid-water cold cloud tops.

Two types of errors can be identified in this study: 1) NWP model error and 2) CRTM error. Examples of NWP model errors are the microphysical errors that occurred in both the 27 June 2005 and the 26 July 2014 cases, which are discussed in detail in previous publications. Results from the above four cases indicated that one feature that was unsupported by observations was
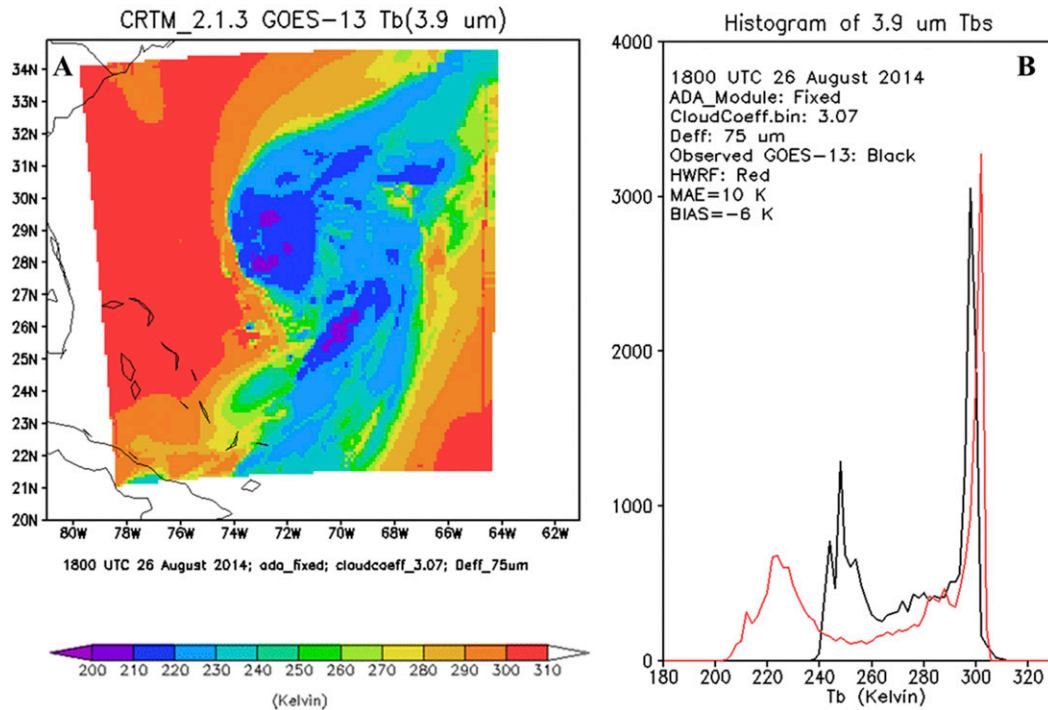

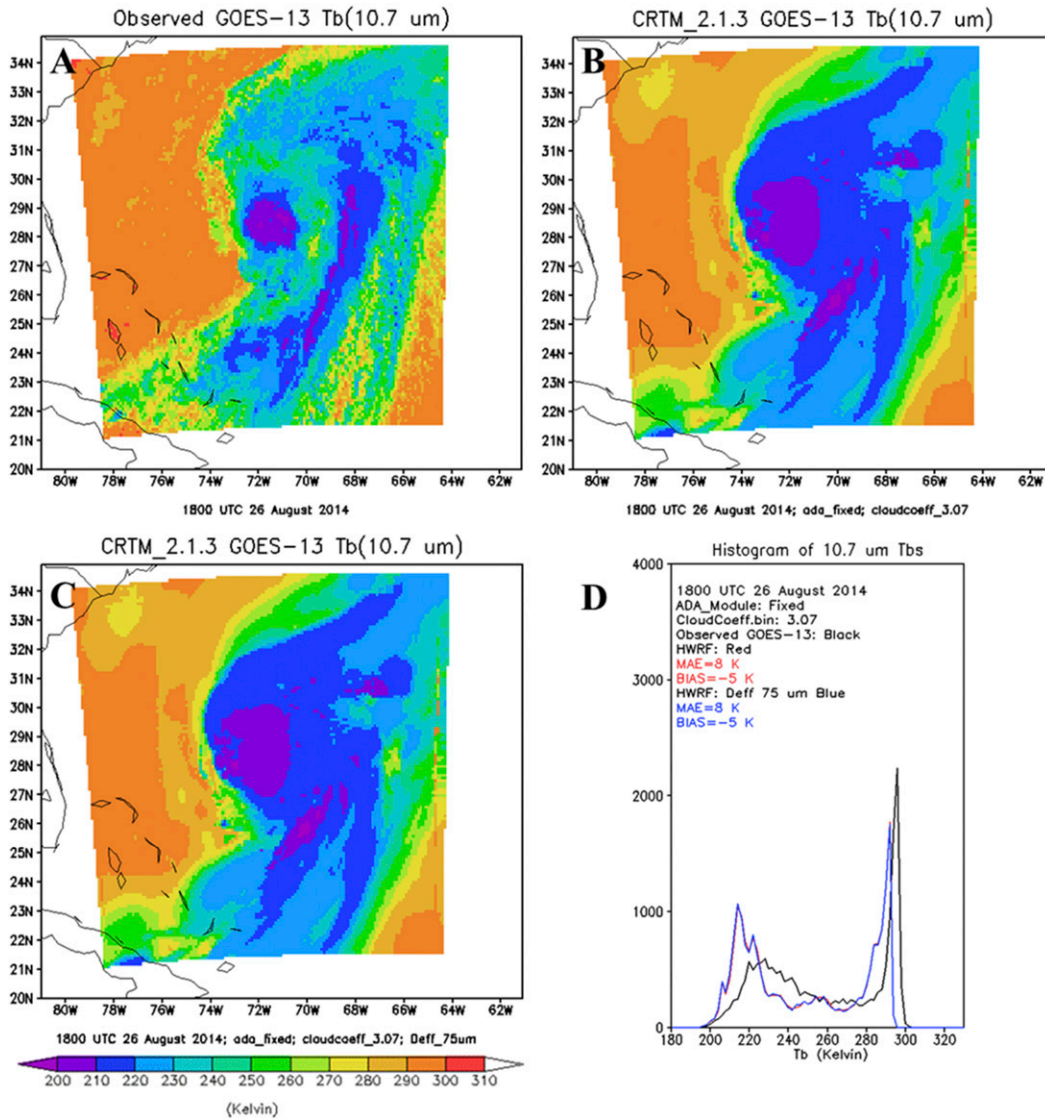FIG. 13. (a) As in Fig. 7d, but with Deff = 75 μm for ice. (b) As in Fig. 8c, but with Deff = 75 μm for ice.

FIG. 14. Remapped *GOES-13* Tbs (K) near 10.7 μm valid at 1800 UTC 26 Aug 2014 from (a) observations and from the CRTM_2.1.3 with (b) ada_fixed and cloudcoeff_3.07, and (c) ada_fixed, cloudcoeff_3.07, and Deff = 75 μm. (d) Histograms, in 2-K bins, of observed (black) and CRTM_2.1.3 with ada_fixed and cloudcoeff_3.07 (red) and with ada_fixed, cloudcoeff_3.07, and Deff = 75 μm (blue). Note that the red and blue curves are nearly identical.

the cold bias of cold solid-water cloud tops. Since this feature was common to imagery from different models, microphysics, and meteorological events, one possible source of an error may be the CRTM itself, as was the case herein. Two errors were identified and resolved with the CRTM: the exclusion of solar reflection and an erroneous optical property LUT. The error associated with solar reflection was first identified by the CRTM team who also provided guidance on the solution. Once solar reflection was included, values of Tbs near 3.9 μm associated with cold cloud tops increased. Unluckily,

values of Tbs increased too much relative to observations. After the inclusion of an updated LUT, values of Tbs near 3.9 μm decreased to near observed values; save the tropical cyclone case. Values of Tbs near 3.9 μm exhibited little change for the tropical cyclone case that was simulated with the operational HWRF system.

One aspect of the generation of synthetic imagery is the coupling of numerical weather prediction model microphysical characteristics and microphysical characteristics used to develop the LUT of optical properties within the CRTM. An inconsistency, as opposed to an

error, may occur when microphysical characteristics differ between an NWP model and the CRTM. That is, the incompatibility between an NWP model and CRTM microphysics could be viewed as simply an incompatibility as opposed to either an NWP model or CRTM error. As stated in section 3, Sieron et al. (2017, 2018) have proposed to generate LUTs for the CRTM that are specific to the microphysics of an NWP model.

MODIS-retrieved particle sizes were used to recompute synthetic imagery for two of the four cases. Particle sizes were replaced with values from MODIS retrievals for the 29 April 2014 case and the 26 August 2014 tropical cyclone event. Values of Tbs near $3.9 \mu m$ showed additional improvement for the 29 April 2014 case when MODIS particle sizes were used. Similar to the above comments about the tropical cyclone case, little if any change in Tbs occurred for cold cloud tops when MODIS particle sizes were used for ice. This result occurred despite a 50% reduction in ice size compared to the fixed size specified for ice in the Ferrier–Aligo microphysics. To demonstrate the sensitivity of values of Tbs, at different wavelengths, to particle sizes, the CRTM was also run near $10.7 \mu m$. Although the impact on the values of Tbs near $10.7 \mu m$ was smaller compared to those near $3.9 \mu m$, there was a slight cooling near $10.7 \mu m$ for the 29 April 2014 case. Results suggest that further investigation of the microphysics for both the 29 April 2014 and 26 August 2014 cases are warranted and are reserved for future work.

Motivation for the study contained herein is in preparation for all-sky radiance assimilation. Although there are many aspects of all-sky radiance assimilation, two will be highlighted here: first, is the integrity of a forward radiative transfer model; in this case, the CRTM. Since the CRTM is part of the NCEP operational data assimilation systems, it is critical to ensure the accuracy of this radiative transfer model for operational all-sky radiance assimilation. Initially, the CRTM, version 2.1.3, was found to produce erroneous Tbs, from solid-water cold cloud tops, near $3.9 \mu m$, which detects both reflected solar and emitted longwave radiation during the day. The following two corrections were made: 1) a coding error that accounted for the inclusion of solar reflection from clouds in ADA_Module.f90 and 2) an update to the optical properties in the lookup table used by the CRTM: from CloudCoeff.bin, version 3.04 to version 3.07. Resolution of the solar reflection error will be included in the publicly released CRTM, version 2.3.0. Consequently, the integrity of both the radiative transfer model, the CRTM (version 2.1.3 herein), and any microphysical scheme in a forecast model are necessary for successful future all-sky radiance assimilation. Perhaps future advancements in numerical weather prediction may benefit from a direct working collaboration between microphysics and data assimilation developers.

REFERENCES

Baum, B. A., P. Yang, A. J. Heymsfield, A. Bansemer, B. H. Cole, A. Merrelli, C. Schmitt, and C. Wang, 2014: Ice cloud single-scattering property models with the full phase matrix at wavelengths from 0.2 to 100μm. *J. Quant. Spectrosc. Radiat. Transfer*, **146**, 123–139, https://doi.org/10.1016/j.jqsrt.2014.02.029.

Bessho, K., and Coauthors, 2016: An introduction to Himawari-8/9—Japan's new-generation geostationary meteorological satellites. *J. Meteor. Soc. Japan*, **94**, 151–183, https://doi.org/10.2151/jmsj.2016-009.

Bikos, D., and Coauthors, 2012: Synthetic satellite imagery for real-time high-resolution model evaluation. *Wea. Forecasting*, **27**, 784–795, https://doi.org/10.1175/WAF-D-11-00130.1.

Clark, A. J., and Coauthors, 2012: An overview of the 2010 Hazardous Weather Testbed Experimental Forecast Program Spring Experiment. *Bull. Amer. Meteor. Soc.*, **93**, 55–74, https://doi.org/10.1175/BAMS-D-11-00040.1.

Cotton, W. R., and Coauthors, 2003: RAMS 2001: Current status and future direction. *Meteor. Atmos. Phys.*, **82**, 5–29, https://doi.org/10.1007/s00703-001-0584-9.

Derber, J. C., and W.-S. Wu, 1998: The use of TOVS cloud-cleared radiances in the NCEP SSI analysis system. *Mon. Wea. Rev.*, **126**, 2287–2299, https://doi.org/10.1175/1520-0493(1998)126<2287:TUOTCC>2.0.CO;2.

Ding, S., P. Yang, F. Weng, Q. Liu, Y. Han, P. Van Delst, J. Li, and B. Baum, 2011: Validation of the community radiative transfer model. *J. Quant. Spectrosc. Radiat. Transfer*, **112**, 1050–1064, https://doi.org/10.1016/j.jqsrt.2010.11.009.

Goodman, S. J., and Coauthors, 2012: The GOES-R Proving Ground: Accelerating user readiness for the next-generation geostationary environmental satellite system. *Bull. Amer. Meteor. Soc.*, **93**, 1029–1040, https://doi.org/10.1175/BAMS-D-11-00175.1.

Grasso, L., and D. Lindsey, 2011: An example of the use of synthetic 3.9 μm *GOES-12* imagery for two-moment microphysical evaluation. *Int. J. Remote Sens.*, **32**, 2337–2350, https://doi.org/10.1080/01431161003698294.

——, ——, K.-S. Lim, A. Clark, D. Bikos, and S. Dembek, 2014: Evaluation of and suggested improvements to the WSM6 microphysics in WRF-ARW using synthetic and observed *GOES-13* imagery. *Mon. Wea. Rev.*, **142**, 3635–3650, https://doi.org/10.1175/MWR-D-14-00005.1.

Han, Y., P. van Delst, Q. Liu, F. Weng, B. Yan, R. Treadon, and J. Derber, 2006: JCSDA Community Radiative Transfer Model (CRTM)—version 1. NOAA Tech. Rep. NESDIS 122, 40 pp.

Heidinger, A. K., C. O'Dell, R. Bennartz, and T. Greenwald, 2006: The successive-order-of-interaction radiative transfer model. *J. Appl. Meteor. Climatol.*, **45**, 1388–1402, https://doi.org/10.1175/JAM2387.1.

Hu, Y. X., B. Wielicki, B. Lin, G. Gibson, S. C. Tsay, K. Stamnes, and T. Wong, 2000: δ-Fit: A fast and accurate treatment of particle scattering phase functions with weighted singular-value decomposition least-squares fitting. *J. Quant. Spectrosc. Radiat. Transfer*, **65**, 681–690, https://doi.org/10.1016/S0022-4073(99)00147-8.

Kleist, D. T., and K. Ide, 2015: An OSSE-based evaluation of hybrid variational–ensemble data assimilation for the NCEP GFS. Part II: 4D EnVar and hybrid variants. *Mon. Wea. Rev.*, **143**, 452–470, https://doi.org/10.1175/MWR-D-13-00350.1.

——, D. F. Parrish, J. C. Derber, R. Treadon, W. S. Wu, and S. Lord, 2009: Introduction of the GSI into the NCEP Global Data Assimilation System. *Wea. Forecasting*, **24**, 1691–1705, https://doi.org/10.1175/2009WAF2222201.1.

Kong, F., and Coauthors, 2007: Preliminary analysis on the real-time storm-scale ensemble forecasts produced as part of the NOAA hazardous weather testbed 2007 spring experiment. *22nd Conf. on Weather Analysis and Forecasting/18th Conf. on Numerical Weather Prediction*, Salt Lake City, UT, Amer. Meteor. Soc., 3B.2, https://ams.confex.com/ams/22WAF18NWP/techprogram/paper_124667.htm.

Liu, Q., and F. Weng, 2006: Advanced doubling-adding method for radiative transfer in planetary atmosphere. *J. Atmos. Sci.*, **63**, 3459–3465, https://doi.org/10.1175/JAS3808.1.

Matricardi, M., F. Chevallier, G. Kelly, and J.-N. Thepaut, 2004: An improved general fast radiative transfer model for the assimilation of radiance observations. *Quart. J. Roy. Meteor. Soc.*, **130**, 153–173, https://doi.org/10.1256/qj.02.181.

Milbrandt, J. A., and M. K. Yau, 2005: A multimoment bulk microphysics parameterization. Part II: A proposed three-moment closure and scheme description. *J. Atmos. Sci.*, **62**, 3065–3081, https://doi.org/10.1175/JAS3535.1.

Minamide, M., and F. Zhang, 2017: Adaptive observation error inflation for assimilating all-sky satellite radiance. *Mon. Wea. Rev.*, **145**, 1063–1081, https://doi.org/10.1175/MWR-D-16-0257.1.

Morrison, H., and J. O. Pinto, 2005: Mesoscale modeling of springtime Arctic mixed-phase stratiform clouds using a new two-moment bulk microphysics scheme. *J. Atmos. Sci.*, **62**, 3683–3704, https://doi.org/10.1175/JAS3564.1.

——, and ——, 2006: Intercomparison of bulk microphysics scheme in mesoscale simulations of springtime Arctic mixed-phase stratiform clouds. *Mon. Wea. Rev.*, **134**, 1880–1900, https://doi.org/10.1175/MWR3154.1.

——, and J. A. Milbrandt, 2015: Parameterization of cloud microphysics based on the prediction of bulk ice particle properties. Part I: Scheme description and idealized tests. *J. Atmos. Sci.*, **72**, 287–311, https://doi.org/10.1175/JAS-D-14-0065.1.

——, G. Thompson, and V. Tatarskii, 2009: Impact of cloud microphysics on the development of trailing stratiform precipitation in a simulated squall line: Comparison of one- and two-moment schemes. *Mon. Wea. Rev.*, **137**, 991–1007, https://doi.org/10.1175/2008MWR2556.1.

Parrish, D. F., and J. C. Derber, 1992: The National Meteorological Center's spectral statistical interpolation analysis system. *Mon. Wea. Rev.*, **120**, 1747–1763, https://doi.org/10.1175/1520-0493(1992)120<1747:TNMCSS>2.0.CO;2.

Reisner, J., R. M. Rasmussen, and R. T. Bruintjes, 1998: Explicit forecasting of supercooled liquid water in winter storms using the MM5 mesoscale model. *Quart. J. Roy. Meteor. Soc.*, **124**, 1071–1107, https://doi.org/10.1002/qj.49712454804.

Saunders, R. W., M. Matricardi, and P. Brunel, 1999: An improved fast radiative transfer model for assimilation of satellite radiance observations. *Quart. J. Roy. Meteor. Soc.*, **125**, 1407–1425, https://doi.org/10.1002/qj.1999.49712555615.

Schmit, T. J., P. Griffith, M. M. Gunshor, J. M. Daniels, S. J. Goodman, and W. J. Lebair, 2017: A closer look at the ABI on the GOES-R series. *Bull. Amer. Meteor. Soc.*, **98**, 681–698, https://doi.org/10.1175/BAMS-D-15-00230.1.

Seemann, S. W., E. E. Borbas, R. O. Knuteson, G. R. Stephenson, and H.-L. Huang, 2008: Development of a global infrared land surface emissivity database for application to clear-sky sounding retrievals from multispectral satellite radiance measurements. *J. Appl. Meteor. Climatol.*, **47**, 108–123, https://doi.org/10.1175/2007JAMC1590.1.

Senf, F., and H. Deneke, 2017: Uncertainties in synthetic Meteosat SEVIRI infrared brightness temperatures in the presence of cirrus clouds and implications for evaluation of cloud microphysics. *Atmos. Res.*, **183**, 113–129, https://doi.org/10.1016/j.atmosres.2016.08.012.

Sieron, S. B., E. E. Clothiaux, F. Zhang, Y. Lu, and J. A. Otkin, 2017: Comparison of using distribution-specific versus effective radius methods for hydrometeor single-scattering properties for all-sky microwave satellite radiance simulations with different microphysics parameterization schemes. *J. Geophys. Res. Atmos.*, **122**, 7027–7046, https://doi.org/10.1002/2017JD026494.

——, F. Zhang, E. E. Clothiaux, L. N. Zhang, and Y. Lu, 2018: Representing precipitation ice species with both spherical and nonspherical particles for radiative transfer modeling of microphysics-consistent cloud microwave scattering properties. *J. Adv. Model. Earth Syst.*, **10**, 1011–1028, https://doi.org/10.1002/2017MS001226.

Skamarock, W. C., J. B. Klemp, J. Dudhia, D. O. Gill, D. M. Barker, W. Wang, and J. G. Powers, 2005: A description of the Advanced Research WRF version 2. NCAR Tech. Note NCAR/TN-468+STR, 88 pp., https://doi.org/10.5065/D6DZ069T.

Tallapragada, V., and Coauthors, 2014: Hurricane Weather Research and Forecasting (HWRF) Model: 2014 scientific documentation. HWRF v3.6a, Developmental Testbed Center, Boulder, CO, 105 pp., https://dtcenter.org/HurrWRF/users/docs/scientific_documents/HWRFv3.6a_ScientificDoc.pdf.

Thompson, G., R. M. Rasmussen, and K. Manning, 2004: Explicit forecasts of winter precipitation using an improved bulk microphysics scheme. Part I: Description and sensitivity analysis. *Mon. Wea. Rev.*, **132**, 519–542, https://doi.org/10.1175/1520-0493(2004)132<0519:EFOWPU>2.0.CO;2.

——, M. Tewari, K. Ikeda, S. Tessendorf, C. Weeks, J. A. Otkin, and F. Kong, 2016: Explicitly-coupled cloud physics and radiation parameterizations and subsequent evaluation in WRF high-resolution convective forecasts. *Atmos. Res.*, **168**, 92–104, https://doi.org/10.1016/j.atmosres.2015.09.005.

Wang, X., D. Parrish, D. Kleist, and J. S. Whitaker, 2013: GSI 3DVar-based ensemble–variational hybrid data assimilation for NCEP Global Forecast System: Single-resolution experiments. *Mon. Wea. Rev.*, **141**, 4098–4117, https://doi.org/10.1175/MWR-D-12-00141.1.

Wu, T.-C., M. Zupanski, L. D. Grasso, P. J. Brown, C. D. Kummerow, and J. Knaff, 2016: The GSI capability to assimilate TRMM and GPM hydrometeor retrievals in HWRF. *Quart. J. Roy. Meteor. Soc.*, **142**, 2768–2787, https://doi.org/10.1002/qj.2867.

——, ——, ——, C. D. Kummerow, and S.-A. Boukabara, 2018: All-sky radiance assimilation of ATMS in HWRF: A demonstration study. *Mon. Wea. Rev.*, https://doi.org/10.1175/MWR-D-17-0337.1, in press.

Wu, W. S., R. J. Purser, and D. F. Parrish, 2002: Three-dimensional variational analysis with partially inhomogeneous covariances. *Mon. Wea. Rev.*, **130**, 2905–2916, https://doi.org/10.1175/1520-0493(2002)130<2905:TDVAWS>2.0.CO;2.

Xue, M., and Coauthors, 2007: CAPS realtime storm-scale ensemble and high-resolution forecasts as part of the NOAA Hazardous Weather Testbed 2007 spring experiment. *22nd Conf. on Weather Analysis and Forecasting/18th Conf. on Numerical Weather Prediction*, Salt Lake City, UT, Amer. Meteor. Soc., 3B.1, https://ams.confex.com/ams/22WAF18NWP/techprogram/paper_124587.htm.

Yang, P., L. Bi, B. A. Baum, K. N. Liou, G. W. Kattawar, and M. Mishchenko, 2013: Spectrally consistent scattering, absorption, and polarization properties of atmospheric ice crystals at wavelengths from $0.2\,\mu m$ to $100\,\mu m$. *J. Atmos. Sci.*, **70**, 330–347, https://doi.org/10.1175/JAS-D-12-039.1.

Zhang, F., M. Minamide, and E. E. Clothiaux, 2016: Potential impacts of assimilating all-sky infrared satellite radiances from GOES-R on convection-permitting analysis and prediction of tropical cyclones. *Geophys. Res. Lett.*, **43**, 2954–2963, https://doi.org/10.1002/2016GL068468.

Zhu, Y., and Coauthors, 2016: All-sky microwave radiance assimilation in NCEP's GSI analysis system. *Mon. Wea. Rev.*, **144**, 4709–4735, https://doi.org/10.1175/MWR-D-15-0445.1.

Zou, X., X. Zhuge, and F. Weng, 2016: Characterization of bias of advanced Himawari imager infrared observations from NWP background simulations using CRTM and RTTOV. *J. Atmos. Oceanic Technol.*, **33**, 2553–2567, https://doi.org/10.1175/JTECH-D-16-0105.1.